

Parametric study on stability and morphology of liquid cone in flow focusing

Kai Mu, Ran Qiao, Jianfeng Guo, Chaoyu Yang, Yanfeng Wu*, Ting Si

Department of Modern Mechanics, University of Science and Technology of China, Hefei 230026, China

ARTICLE INFO

Article history:

Received 10 August 2020

Revised 28 October 2020

Accepted 5 November 2020

Available online 11 November 2020

Keywords:

Flow focusing

Liquid cone

Parametric study

Recirculation flow

ABSTRACT

A parametric study on the stability and morphology of the liquid cone in a flow focusing process is carried out through experimental and numerical methods. For the numerical simulations, we solve the Navier-Stokes equations coupled with a diffuse interface method. A scaling analysis which considers the competition between the viscous shear stress and the interfacial tension force is proposed, showing the effect of flow rates, geometrical parameters and liquid physical properties on the cone instability. The experimental and numerical results validate the scaling law and further show the effects of parameters on the cone morphology. We study the flow fields inside the liquid cone, with emphatic focus on the recirculation flow pattern which occurs at relatively high viscosity ratio between the focusing and the focused liquids. The occurrence of recirculation flow is close related to the tangential velocity distribution at both sides of the cone interface, and the change of flow rates and geometrical parameters is found to significantly affect the size of the recirculation flow. This study is expected to give a guidance to the optimization of process parameters in flow focusing system, which would contribute to the formation of a stable cone-jet structure and the production of microdroplets with high throughput.

© 2020 Elsevier Ltd. All rights reserved.

1. Introduction

Droplet-based microfluidics is a significant method to fabricate droplets, bubbles and capsules at microscales (Barrero and Loscertales, 2007; Gañán-Calvo et al., 2013). Among the abundant microfluidic strategies, the most popular ones are the two-dimensional microchannels and the axisymmetric glass microcapillaries, in which the multi-phase fluids flow through the well designed channel with confined boundaries and finally break up into droplets due to interface instabilities (Anna, 2016; Zhu and Wang, 2017; Pang et al., 2019; Zhang et al., 2019; Zeguai et al., 2020). Due to the relatively low flow velocities in these microfluidic systems, the Weber number (We) and Reynolds number (Re) are quite small; therefore, the droplets are produced at a low frequency under the viscosity-dominated regime. Meanwhile, the existence of channel boundary leads to the wettability effect and sometimes brings limitations on the selection of fluids (Si et al., 2017). To realize the droplet production with high throughput, one of the capillary flows called flow focusing (FF) has been put forward in the past two decades. In FF, a cuspidal cone forms upstream the focusing orifice, and a jet emits through the cone tip and continuously generate microdroplets downstream the orifice in an open space

(Gañán-Calvo, 1998; Wang et al., 2020; Blanco-Trejo et al., 2020). The liquid jet in FF system operates at relatively high We and Re due to the large volume flux of fluids, and the droplet generations are dominated by the inertia force and the interfacial tension. In recent years, FF has also been generalized with complex geometries to fabricate compound droplets with different geometries and functions, showing wide feasibility of the FF technique in various applications (Si et al., 2015; 2016; Wu et al., 2018; Mu et al., 2020).

In previous studies, the FF has been divided into three groups according to the selection of focused and focusing fluids, i.e., liquid in gas (LG), gas in liquid (GL) and liquid in liquid (LL). Various flow regimes have been found in experiments, in which the jetting and dripping modes are the most typical, either in the LG-FF (Si et al., 2009; 2010), or in the LL-FF (Gañán-Calvo and Riesco-Chueca, 2006; Mu et al., 2018a; 2019). In the jetting mode, a stable liquid cone forms upstream the focusing orifice with a cylindrical jet emits downstream the orifice; while in the dripping mode, no jet can be observed and the droplets are formed right at the exit of orifice with either a stable or an unstable cone. The spatio-temporal linear instability analysis on evolutions of interface perturbation has shown that the jetting mode is dominated by the convective instability; while the dripping mode is dominated by the absolute instability (Eggers and Villermaux, 2008; Chattopadhyay and Gañán-Calvo, 2019). In GL-FF, only the dripping mode can be observed in experiments as the flow is dominated by

* Corresponding author.

E-mail address: wuyf@ustc.edu.cn (Y. Wu).

the absolute instability invariably (Gañán-Calvo and Gordillo, 2001; Gordillo et al., 2001). Generally, the dripping mode is advantageous to produce droplets with high monodispersity (Cruz-Mazo et al., 2016; Mu et al., 2019). However, the throughput in dripping mode is low as the flow operates at relatively low flow rates (Christopher and Anna, 2007; Nunes et al., 2013). On the contrary, the jetting mode can generate droplets with much smaller size and higher productivity under a favourable droplet uniformity. Recently, the external actuation has also been applied on the liquid jet to realize the active control of droplet generation, which is able to manipulate the size and throughput of droplets and enhance the droplet monodispersity significantly (Mu et al., 2018b; Yang et al., 2019).

It should be emphasized that a stable cone in FF is the prerequisite condition for the formation of the liquid jet downstream and is crucial for the efficiency on droplets production. More importantly, the cone also serves as a filter which is able to damp the perturbation upstream and enhance the stability of the jet (Mu et al., 2018b). The characteristics of the cone instability have been studied for the LG-FF process. It is found that a decrease on the flow rate of the focused liquid would result in the vibrating behavior of the cone (Montanero et al., 2011), and the decrease of pressure difference of the focusing gas stream would ultimately cause the adhesion of the focused liquid to the orifice (Si et al., 2009). It is also observed that when the distance between the capillary tube and the focusing orifice is very close, the flow burring regime occurs as the local velocity of the gas stream is very fast, which causes the liquid atomization at the cone (Gañán-Calvo, 2005; Zhao et al., 2019). Furthermore, the numerical simulations reveal that a recirculation flow pattern may occur inside the liquid cone under certain conditions, and the size of the recirculation flow grows with the decrease of focused flow rate (Herrada et al., 2008; Gañán-Calvo et al., 2011). The recirculation flow is regarded as the omen for the transition from the stable to the unstable cones. Comparing with the LG-FF process where the liquid phase is driven by a much faster gas stream, the LL-FF operates at a relatively gentle environment where the velocities of double liquids ranges at the same order. Despite of the existing studies on the liquid cone, a systematic considerations for the effects of various parameters (e.g. device geometry, liquid flow rates and physical properties) on the stability, morphology and flow field of the cone are still desired, especially for the LL-FF system. These limitations motivate the present work.

In this work, we carry out a systematic parametric study on the liquid cone in the LL-FF process. Firstly, a scaling law is performed to show the effects of various parameters on the stability of the liquid cone. The theoretical prediction is validated by experiments and numerical simulations, which further considers the effects of parameters on the cone morphology. Then, we study the flow fields inside the liquid cone through numerical simulations, with special attention to the recirculation flow characteristics which occurs at relatively high viscosity ratio between the focusing and focused liquids. Quantitative velocity profiles across the cone interface are given to show the mechanisms for the occurrence of recirculation flow. Moreover, we study the effect of flow rates and geometric parameters on the size of the recirculation flow. Finally, main conclusions are drawn.

2. Experimental and numerical methods

The experimental platform of FF is constituted by a capillary tube (with inner and outer diameters D and D_o) and a sealed chamber with an orifice (with diameter d and thickness T) at the bottom facing the capillary tube. The distance between the tube exit and the focusing orifice is denoted by H . The experimental setup is analogous to that described in our previous studies (Mu et al., 2018a; 2019). We utilize a syringe pump (WK-101P, China)

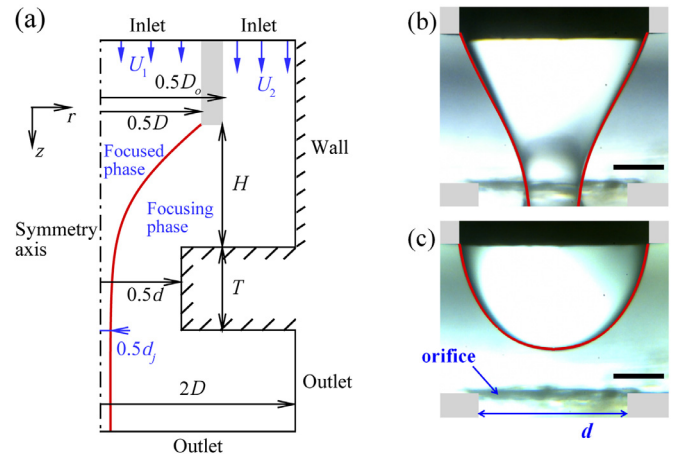


Fig. 1. (a) Computational domain showing the axisymmetric geometry of FF, where U_1 and U_2 denotes the inlet flow velocities of focused and focusing phases, respectively. Comparison between the experimental and numerical results for (b) the stable cone at the liquid flow rates $Q_1=150\text{ml/h}$ and $Q_2=1400\text{ml/h}$ and (c) the unstable cone at the liquid flow rates $Q_1=20\text{ml/h}$ and $Q_2=1400\text{ml/h}$. The numerical cone profiles (lines) are superposed on the experimental results. Scale bar: $300\mu\text{m}$.

to supply the focused liquid (with density ρ_1 , dynamic viscosity μ_1 , flow rate Q_1 and averaged inlet velocity U_1) into the capillary tube and use another one to provide the focusing liquid (with density ρ_2 , dynamic viscosity μ_2 , flow rate Q_2 and averaged inlet velocity U_2) into the chamber. As the focused and focusing liquids converge at the orifice, a liquid cone can be formed between the capillary tube and the orifice, and the fluid interface will ultimately break up into microdroplets downstream due to flow instabilities. We record the evolution of interface with a high-speed camera (Photron, Fastcam Mini AX, Japan) accompany with a microscope (Leica Z16 APO, Germany) under the illumination of an intense light source (Sumita LS-M352, Japan) from the other side of the chamber. In our experiments, we set the geometric parameters as: $D=1050\mu\text{m}$, $D_o=1250\mu\text{m}$, $d=840\mu\text{m}$, $T=450\mu\text{m}$, and H varies between 300 and $1700\mu\text{m}$. Silicone oil and distilled water are selected as the focused and focusing liquids, respectively. All the experiments are carried out at room temperature $T=25^\circ\text{C}$, where the liquid physical parameters are $\rho_1=965\text{kg/m}^3$, $\mu_1=0.005\text{Pa}\cdot\text{s}$, $\rho_2=995\text{kg/m}^3$, and $\mu_2=0.001\text{Pa}\cdot\text{s}$; the oil-water interfacial tension is $\sigma=33.2\text{mN/m}$.

According to the experimental configuration, the computational domain is shown in Fig. 1(a), in which the geometrical parameters, boundary conditions, and averaged inlet flow velocities U_1 and U_2 are also indicated. In numerical simulations, we solve the Navier-Stokes equations coupled with a diffuse interface method, where the interface is represented by the volume fraction of the liquid (i.e. C), and its time evolution is governed by the Cahn-Hilliard equation (Zhao, 2012), which captures the interface position accurately and ensures the balance of the interface,

$$\frac{\partial C}{\partial t} + \nabla \cdot (\mathbf{u}C) = \frac{1}{Pe} \nabla^2 \psi, \quad (1)$$

where the chemical potential ψ is defined as,

$$\psi = C^3 - 1.5C^2 + 0.5C - Cn^2 \nabla^2 C, \quad (2)$$

and the Cahn number Cn is a dimensionless measurement on the thickness of diffuse interface. In numerical simulations, the interface is represented by the contour $C=0.5$ and Cn is set to $0.5\Delta x$, where Δx is the mesh size. In order to ensure the convergence of the diffuse interface, we choose the Peclet number $Pe = \alpha/Cn$ with α as a constant coefficient to sharpen the interface as the value of Cn gradually decreases (Magaletti et al., 2013). As suggested by

the previous works (Ding et al., 2007; Mu et al., 2018b; 2020), the value of $\alpha = 1$ (i.e., $Pe = 1/Cn$) is given in this study.

The motion of the focused and focusing liquids is governed by the dimensionless Navier-Stokes equations:

$$\rho \left(\frac{\partial \mathbf{u}}{\partial t} + \mathbf{u} \cdot \nabla \mathbf{u} \right) = -\nabla p + \frac{1}{Re} \nabla \cdot [\mu (\nabla \mathbf{u} + \nabla \mathbf{u}^T)] + \frac{\mathbf{f}_s}{We}, \quad (3)$$

$$\nabla \cdot \mathbf{u} = 0, \quad (4)$$

where $\mathbf{f}_s = 6\sqrt{2}\psi \nabla C/Cn$ is the surface tension force, $\mu = C + (1 - C)r_\mu$ and $\rho = C + (1 - C)r_\rho$ are the dimensionless averaged viscosity and density, and $r_\mu = \mu_2/\mu_1$ and $r_\rho = \rho_2/\rho_1$ are the viscosity and density ratios between the focusing and focused liquids, respectively (Ding et al., 2007). In our simulations, we choose D and U_1 as the characteristic length and velocity, and further define the Reynolds number as $Re = \rho_1 U_1 D / \mu_1$ and the Weber number as $We = \rho_1 U_1^2 D / \sigma$. For the convenience of analysis, we also refer to the Ohnesorge number $Oh = \mu_1 / \sqrt{\rho_1 \sigma D}$ and the flow rate ratio $q = Q_2/Q_1$ between the focusing and focused liquids. Our experiments correspond to the dimensionless parameters $Oh=0.026$, $r_\mu=0.2$ and $r_\rho=1.031$. The values of Re , We and q depend on the liquid flow rates. For the numerical simulations, the effects of liquid viscosities and interfacial tension are also studied through changing r_μ and Oh , respectively.

In the numerical simulations, a uniform Cartesian mesh is used in the $z-r$ plane, where z and r denotes the axial and radial directions, respectively. The computational domain is set with a certain size of $2D \times 5D$, which is adequate for the evolutions of liquid cone, and a mesh size of $\Delta x = 1/200D$ is employed for sufficient calculating accuracy. The boundary conditions are given as follows: symmetrical conditions $u = 0$ and $\partial v / \partial r = 0$ at $r = 0$, where u and v denote the z - and r - components of the flow velocities, respectively; non-slipping conditions $u = 0$ and $v = 0$ at the solid wall; $v = v_{in}$ and $u = 0$ at the fluid inlet, where v_{in} is a prescribed velocity according to the flow rate; and $\partial u / \partial z = \partial v / \partial z = 0$ at the outlet. We also apply the wetting conditions at the contact line to serve as the boundary condition for C at the solid wall (Ding and Spelt, 2007). More details of numerical simulations can be found in Ding et al. (2007) and Liu et al. (2016). The numerical code has been successfully validated in previous studies on the liquid jet breakup in FF system (Mu et al., 2018b; 2018a; 2019; 2020). In this study, we present a comparison between the numerical results and experimental observations for the liquid cone. Fig. 1(b) shows the profiles for a stable cone at the flow rates $Q_1=150$ ml/h and $Q_2=1400$ ml/h, which correspond to $We=0.087$ and $q=9.3$, respectively. Meanwhile, Fig. 1(c) shows the snapshot image for a vibrating cone at the flow rates $Q_1=20$ ml/h and $Q_2=1400$ ml/h ($We=0.002$ and $q=70$). Clearly, a good agreement can be reached between the results, either for the stable or the unstable cone.

3. Results and discussions

3.1. Scaling analysis on the cone instability

It has been indicated that the instability of the liquid cone upstream the orifice corresponds to a global instability problem (Montanero et al., 2011). For the globally stable mode, the cone is able to maintain a temporally steady profile; while for the globally unstable flow, the cone will vibrate periodically between the orifice and the capillary tube. We present a scaling analysis here to estimate the effect of various parameters on the cone instability. Generally, the formation of a liquid cone is closely related to the competition between the viscous shear stress and the interfacial tension force on the interface. The order of viscous shear stress τ_s

which stretches the interface can be estimated as,

$$\tau_s \sim \frac{\mu_2 \bar{U}_2}{d}, \quad (5)$$

where $\bar{U}_2 \approx Q_2 / (\pi d H)$ reflects the average velocity of the focusing liquid close to the cone interface. It is noteworthy that the average velocity is appropriately calculated through dividing the flow rate Q_2 to the lateral area of the zone between the orifice and the capillary tube, suggesting that the geometrical parameters d and H plays a crucial role on the focusing velocity and D plays a secondary effect. The form of shear stress is very similar to that which has been utilized to estimate the shear force in two-dimensional microfluidic systems (Anna, 2016; Anna and Mayer, 2006; Lee et al., 2009). The interfacial tension stress τ_σ which try to suppress the deformation of the interface is estimated as,

$$\tau_\sigma \sim \frac{\sigma}{d_j}, \quad (6)$$

where d_j is the diameter of the the liquid jet measured at the orifice exit, as sketched in Fig. 1. If a stable cone is established, τ_s should overcome τ_σ at the orifice. Then the ratio between τ_s and τ_σ can be expressed as,

$$\frac{\tau_s}{\tau_\sigma} \sim \frac{\mu_2 \bar{U}_2}{d} \cdot \frac{d_j}{\sigma}. \quad (7)$$

Previous studies have shown that an approximated average velocity of the focused and focusing liquid would be reached downstream the orifice due to the viscous momentum diffusion, which gives the prediction of jet diameter through volume conservation (Mu et al., 2018a; Castro-Hernandez et al., 2009; Gañán-Calvo and Riesco-Chueca, 2006),

$$d_j \approx d \left(\frac{Q_1}{Q_1 + Q_2} \right)^{\frac{1}{2}} = d \left(\frac{1}{1 + q} \right)^{\frac{1}{2}}. \quad (8)$$

Under the assumption of $Q_1 \ll Q_2$, Eq. (7) can be finally written as,

$$\frac{\tau_s}{\tau_\sigma} \sim \frac{\mu_2}{\sigma} \cdot \frac{(Q_1 \cdot Q_2)^{\frac{1}{2}}}{d \cdot H}. \quad (9)$$

The dimensionless form of Eq. (9) corresponds to,

$$\frac{\tau_s}{\tau_\sigma} \sim \frac{r_\mu \cdot Oh \cdot (We \cdot q)^{\frac{1}{2}}}{d \cdot H}. \quad (10)$$

It can be found that the value of τ_s/τ_σ is proportional to the square root of Q_1 and Q_2 (nondimensionalized as We and q), proportional to μ_2 (nondimensionalized as r_μ), and inversely proportional to σ (nondimensionalized as Oh) and the geometrical parameters (d and H). As the values of Q_1 , Q_2 and μ_2 increase, or that of σ , d and H decreases, the viscous shear stress will play a more crucial role in stretching the interface into a tapered shape, thus promoting the stability of the cone.

3.2. Effect of parameters on the cone stability

In this section, we study the effect of process and geometrical parameters on the stability and morphology of the cone. The effect of focused flow rate Q_1 on the liquid cone is shown in Fig. 2(a), in which the experimental and numerical results locate at the upper and lower part of each subgraph, respectively. According to our definition of the dimensionless parameters, it is noteworthy that the variation of Q_1 at a certain Q_2 corresponds to the change of We at a certain value of $We \cdot q^2$. It is observed that under a critical value of Q_1 , the cone is unstable and vibrates between the orifice and the capillary tube. Meanwhile, the streamlines inside the cone would penetrate the interface due to the unsteady flow characteristics, as shown by the numerical results. An increase of Q_1

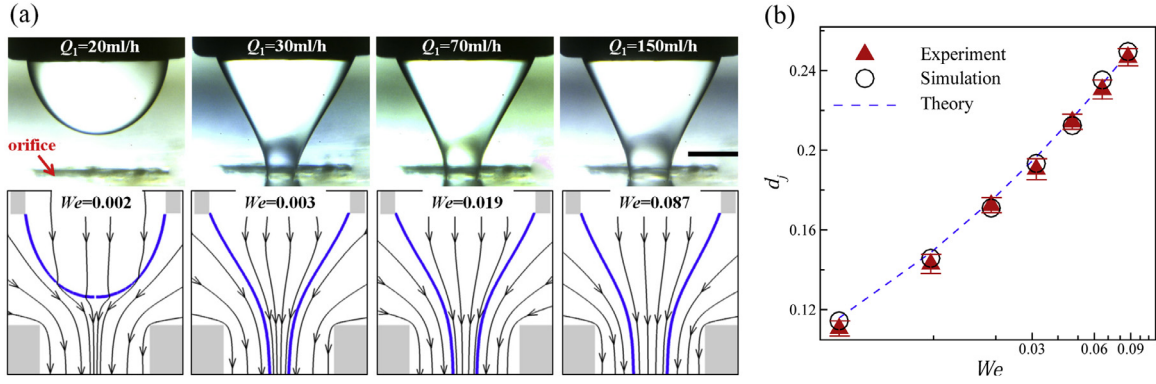


Fig. 2. (a) Cone profiles and streamlines as Q_1 changes at certain $Q_2=1400$ ml/h, corresponding to the variation of We at certain $We \cdot q^2=7.6$. The blue lines represent the interface. Scale bar: 400 μ m. (b) The dimensionless jet diameter d_j as We changes, the dashed line denotes the theoretical prediction of Eq. (8).

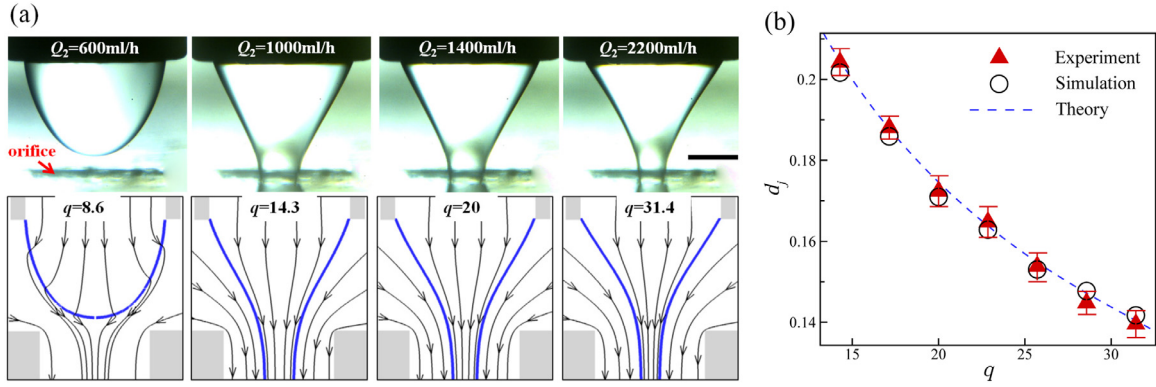


Fig. 3. (a) Cone profiles and streamlines as Q_2 decreases at certain $Q_1=70$ ml/h, corresponding to the variation of q at certain $We=0.019$. The blue lines represent the interface. Scale bar: 400 μ m. (b) The dimensionless jet diameter d_j as q changes, the dashed line denotes the theoretical prediction of Eq. (8).

gradually leads to a stable cone, and the streamlines both inside and outside the cone keep almost stationary. Once the cone gets stable, a steady jet can be formed downstream the orifice with a certain diameter at the orifice exit. Fig. 2(b) plots the jet diameters measured at the orifice exit in experiments and simulations as We (Q_1) varies, which shows a good agreement with the theoretical results of Eq. (8). Due to the random disturbance in experiments, the jet diameter would vary slightly. Therefore, the average values of d_j and its variation ranges are denoted by the solid symbols and the error bars, respectively. It is notable that although the jet diameters are not directly expressed by We in Eq. (8), the singly variation of Q_1 (We) would change the value of q ($\sim We^{-1/2}$) and therefore manipulate the jet diameters. Although the change of We affects the jet diameters, the overall profiles of the cone interface would not change significantly (see Fig. 2a). Fig. 3(a) considers the effect of Q_2 on the liquid cone, which correspond to a change of q at a certain value of We . Similar to the effect of Q_1 , it is observed that the cone would vibrate when Q_2 is lower than a critical value, and becomes stable as Q_2 gradually increases. Once the liquid cone gets stable, the continuous increase of Q_2 would not affect the overall shape of the cone significantly, but would decrease the jet diameters downstream the cone. The jet diameters measured in experiments and numerical simulations as q (Q_2) varies are given in Fig. 3(b), which also shows a good agreement with the theoretical results of Eq. (8).

We also consider the effects of geometrical parameters on the liquid cone, including the distance H between the capillary tube and the orifice, the orifice diameter d and the capillary tube diameter D . Fig. 4(a) reveals that H has a huge influence on the stability and morphology of the cone. When H is relatively large, the cone will present an unsteady vibrating manner. As H gradually

decreases, the cone is able to maintain a stable profile. Moreover, it is observed that the cone will gradually transfer from a convex shape at high H to a concave shape at low H . The reason lies in that as the flow velocity far from the focusing orifice is relatively low, the interface would present a droplet-like convex shape due to the effect of interfacial tension. However, the shear force close to the orifice will significantly stretch the interface and thus present a concave shape when H is low. The jet diameters under different H are shown in Fig. 4(b), suggesting that H would not affect d_j observably, and the results are consistent with the theoretical predictions.

Due to the integration of our experimental device, it is inconvenient to change d or D optionally. Therefore, the effects of d and D are studied only through numerical simulations, as shown in Figs. 5(a) and (b), respectively. It is observed in Fig. 5(a) that the cone is unstable at a large d as the flow velocity of the focusing liquid close to the orifice is relatively low, and the shear force is insufficient to stretch the interface to a steady profile. A decrease of d is able to stabilize the liquid cone and also decrease the jet diameters, as shown in Fig. 5(c). Clearly, d_j decreases linearly with d , and the numerical results agree well with the theoretical prediction of Eq. (8). The variation of D is considered in Fig. 5(b). It is found that the increase of D would significantly affect the cone morphology, but would not affect the instability of the cone as the shear effect of the focusing liquid keeps almost constant at the orifice for certain d and H . Meanwhile, the jet diameter is not affected by D , as shown in Fig. 5(d).

We also consider the effects of liquid physical properties, μ_2 and σ (nondimensionalized as r_μ and Oh , respectively), which have been predicted to play a significant role on the cone instability. It is notable that the variation on selection of liquids in

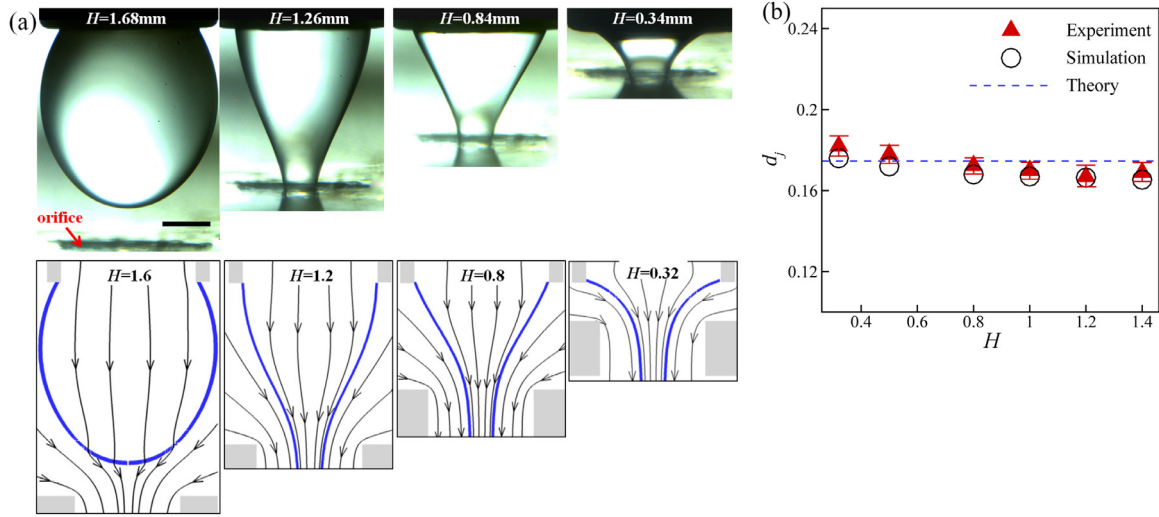


Fig. 4. (a) Cone profiles and streamlines as H varies at certain flow rates of $Q_1=70\text{ml/h}$ and $Q_2=1400\text{ml/h}$ ($We = 0.019$ and $q=20$). The blue lines represent the interface. Scale bar: $400\mu\text{m}$. (b) The dimensionless jet diameter d_j as H changes, the dashed line denotes the theoretical prediction of Eq. (8).

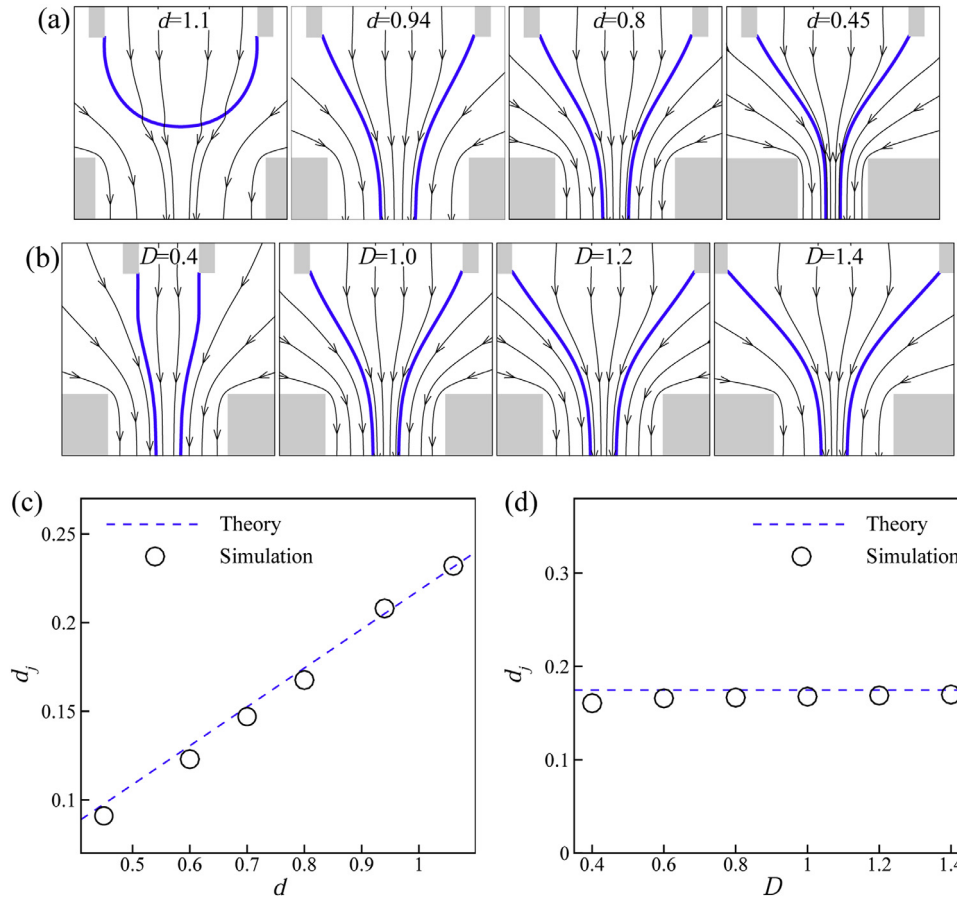


Fig. 5. Numerical cone profiles (represented by the blue lines) and streamlines as (a) the orifice diameter d and (b) capillary tube diameter D varies at the flow rates $We = 0.019$ and $q=20$. The dimensionless jet diameter d_j as d or D singly changes is shown in (c) and (d), and the dashed line is the theoretical law of Eq. (8).

experiments would generally change the liquid viscosity and interfacial tension simultaneously; therefore, the numerical results are utilized here. Fig. 6(a) shows the cone morphology under different Oh . When the value of Oh is low (i.e. $Oh=0.013$), which corresponds to a high value of σ , the cone presents an unstable behavior due to the dominance of interfacial tension. As Oh gradu-

ally increases, which corresponds to the decrease of σ , the shear force is able to overcome the interfacial tension and a stable cone can be established. The variation of r_μ is shown in Fig. 6(b). When r_μ (μ_2) is low, the cone vibrates as the shear force is insufficient to overcome the interfacial tension. The increase of r_μ gradually leads to the stable cone. It is observed dramatically that at a large

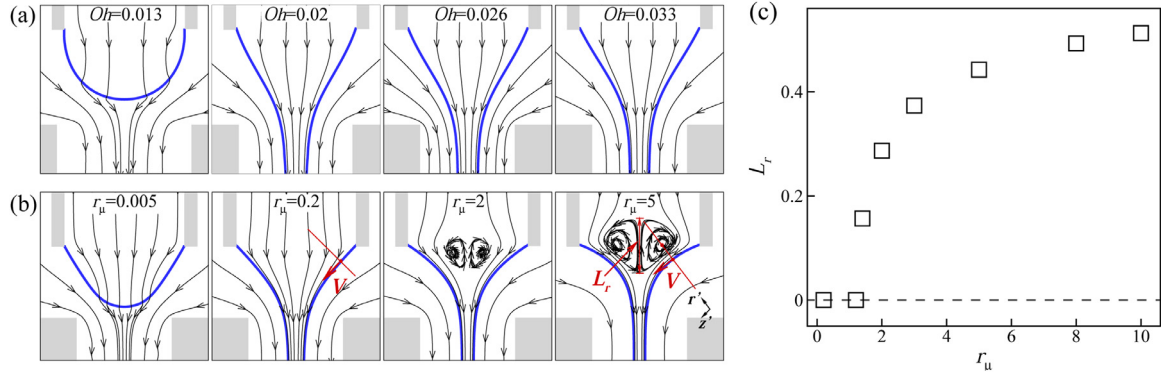


Fig. 6. Numerical cone profiles (represented by the blue lines) and streamlines as (a) Oh varies at $We = 0.019$ and $q=20$, and (b) r_μ varies at $We = 0.008$ and $q=35$. (c) Length of the recirculation cell L_r at different r_μ .

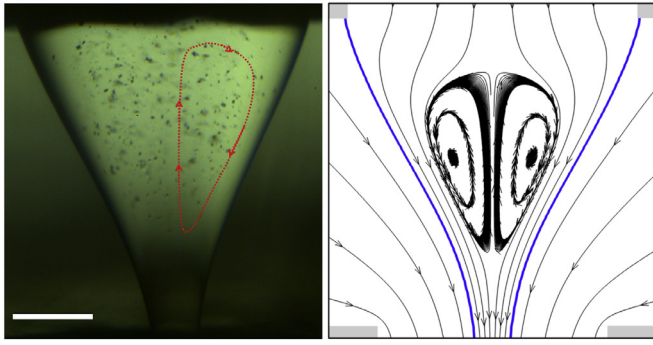


Fig. 7. Experimental visualization of RC through particle tracing method and the corresponding numerical results. The dimensionless parameters are: $We=0.003$, $q=67$, $Oh=0.0034$ and $r_\mu=2.04$. Scale bar: $300\mu m$.

r_μ (e.g. $r_\mu=2$ and 5), a recirculation flow pattern would occur inside the cone. In the recirculation cell (RC), the flow direction in the symmetrical axis is opposite to that in the capillary tube. The RC is temporally steady with its size not varying, suggesting that there is no exchange of liquid inside and outside of the RC; therefore, the RC can be characterized as a ‘dead water region’. In order to show the dynamical flow characteristics of the RC, we mark two groups of particles either inside or outside the RC and track the evolutions of these particles, as shown in Video S1 of the supplementary material. It is clear seen that the particles inside the RC flow upstream close to the symmetry axis due to the back-flow, and the particles outside flow around the RC downstream. Fig. 6(c) further shows the length L_r of RC measured at the symmetry axis (see the definition in the right sub-graph in Fig. 6b) as r_μ changes, which suggests that L_r will gradually increase with r_μ increasing and therefore a larger RC occurs inside the cone.

In this work, we also carry out experiments considering the situations of high r_μ to visualize the RC inside the liquid cone. Due to the design of our FF device, the focusing liquid is constantly selected as distilled water; therefore, we choose silicone oil with very low viscosity (dynamic viscosity $\mu_1=0.00049$ Pa.s) as the focused liquid, which correspond to a viscosity ratio of $r_\mu=2.04$. In such combination of liquids, $Oh=0.0034$. For the visualization of flow fields, we add tracing particles (hollow glass beads with average diameters $20\mu m$) in the focused liquid, and record the motion of particles through high speed camera. Fig. 7 shows the experimental results at the flow rates $Q_1=30$ ml/h and $Q_2=2000$ ml/h ($We=0.003$ and $q=67$). It is clearly observed that RC exists inside the cone and causes the backflow and rotation motion of the trac-

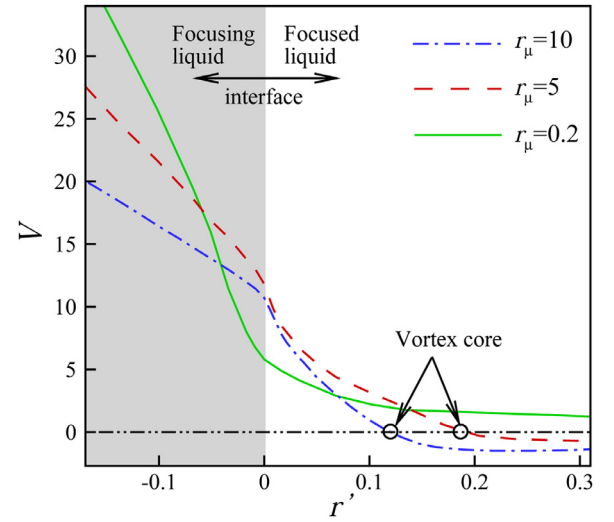


Fig. 8. Distributions of tangential velocity along the r' direction at $r_\mu=0.2, 5$ and 10 , where the white and the shadow region denote the directions inside and outside the cone interface, respectively.

ing particles, as sketched by the dashed line. The dynamical characteristic of the RC can be seen in Video S2 of the supplementary material. It is noteworthy that the light refraction across the interface will cause distortion for the observation of particle movement; therefore, the size of RC is hard to be accurately measured in experiments. Fig. 7 also gives the corresponding numerical results for comparison, which verifies the existence of RC. Moreover, the numerical simulation is able to give the accurate size of RC and the quantitative velocity distributions inside the cone. Overall, the numerical results present a good agreement with the experiments, either for the interface profiles or the flow fields inside the liquid cone.

3.3. Analysis on the recirculation flow

In order to study the mechanisms on the formation of RC under a large r_μ , we start from the vortex core of the RC (corresponding to zero flow velocity) and draw a perpendicular to the cone interface, and extract the tangential velocity V both inside and outside the cone, as sketched in Fig. 6(b) for the case $r_\mu=5$. For comparison, we also extract the tangential velocity for the case $r_\mu=0.2$ at the same z position. The distributions of tangential velocity are shown in Fig. 8, which considers the situations $r_\mu=10, 5$ and 0.2 , respectively. For the case $r_\mu=10$ and 5 , as the viscosity of the

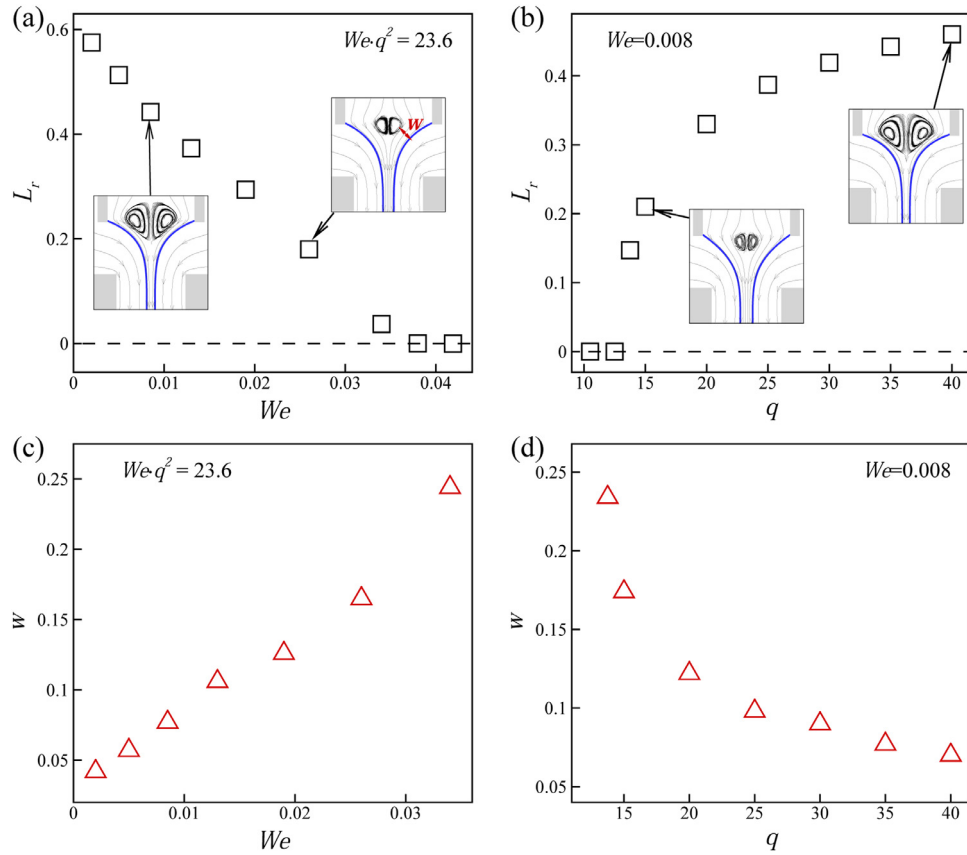


Fig. 9. Length of recirculation cell L_r and gaps between the recirculation cell and the interface w as flow rate varies under $r_\mu=5$, where (a) and (c) We changes at certain $We \cdot q^2=23.6$, and (b) and (d) q changes at certain $We=0.008$.

focused liquid is much lower than that of the focusing liquid, the velocity gradient inside the cone would be obviously larger than that outside the cone in order to ensure the balance of shear force on both sides of the interface. Therefore, the velocity inside the cone drops quickly and becomes opposite some distance inside, which leads to the recirculation flow pattern. However, for the case $r_\mu=0.2$, as the viscosity of the focused liquid is much higher than that of the focusing liquid, the velocity gradient inside the interface is much smaller than that outside the interface, and the drop of velocity inside the cone is relatively gentle without reversion of the flow direction. The results in Fig. 8 reveal that a higher r_μ can promote the descend of tangential velocity inside the liquid cone, which therefore contributes to the occurrence and of RC with a larger size.

Under a relatively high viscosity ratio, the liquid flow rates and geometrical parameters would also influence the size of RC as they affect the local velocity of the liquid cone. The effect of flow rates on the length of RC is shown in Fig. 9, under the viscosity ratio $r_\mu=5$. Fig. 9(a) shows that an increase of We under a certain $We \cdot q^2$ (corresponding to the increase of Q_1 under a certain Q_2) will gradually decrease the length of RC and finally eliminate the RC (i.e. $L_r=0$). Moreover, a larger We leads to a smaller gap size w (sketched in Fig. 9a) between the boundary of RC and the cone interface, as shown in Fig. 9(c). Likewise for the situations as q decreases under a certain We (corresponding to the decrease of Q_2 under a certain Q_1), where the length L_r of RC increases while the gap size w between the RC and the interface decreases with q , as shown in Figs. 9(b) and (d), respectively. Based on the understanding that the size of RC is closely related to the balance of shear force on the cone interface, we can qualitatively give the physical explanation on the effect of focused and focusing flow rates.

Since the decrease of Q_1 is able to decrease the average velocity of the focused liquid, in order to balance the shear force on the cone interface, the RC has to enlarge its size (i.e. a larger L_r) and decrease the effective flow area of the focused liquid inside the cone to maintain the local velocity close to the interface, which therefore results in a smaller w . Similarly, the increase of Q_2 increases the velocity of the focusing liquid outside the cone, which would increase of local velocity inside the interface in order to ensure the balance the shear force. Therefore, the size of RC increases while the gap between the RC and interface decreases with Q_2 increasing.

The effect of geometrical parameters on the recirculation flow is numerically studied in Fig. 10. Fig. 10(a) shows that the length L_r of RC would decrease as the distance H between the capillary tube and orifice gradually increases. If H is larger than a critical value (e. g. $H \leq 1.4$), no RC can be observed. Moreover, the gap size w between the RC and the interface increases with H , as shown in Fig. 10(d). On the contrary, the increase of capillary tube diameter D will increase the length L_r of the RC and also decrease the gap w between the RC and the interface, as shown in Figs. 10(b) and (e), respectively. Figs. 10(c) and (f) consider the effect of orifice diameter d , showing that the increase of d only slightly decrease the L_r and increase the w . The physical reason on the effect of geometrical parameters can be explained as follows: the decrease of H would increase the velocity of focusing liquid during the converge stage close to the orifice, and the increase of D can decrease the average velocity of the focused liquid in the capillary tube; therefore, a larger RC and smaller gap size can be promoted to increase the local velocity close to the interface inside the cone, which contributes to the force balance of shear stress on the interface. However, the decrease of d would increase the velocities of focused and

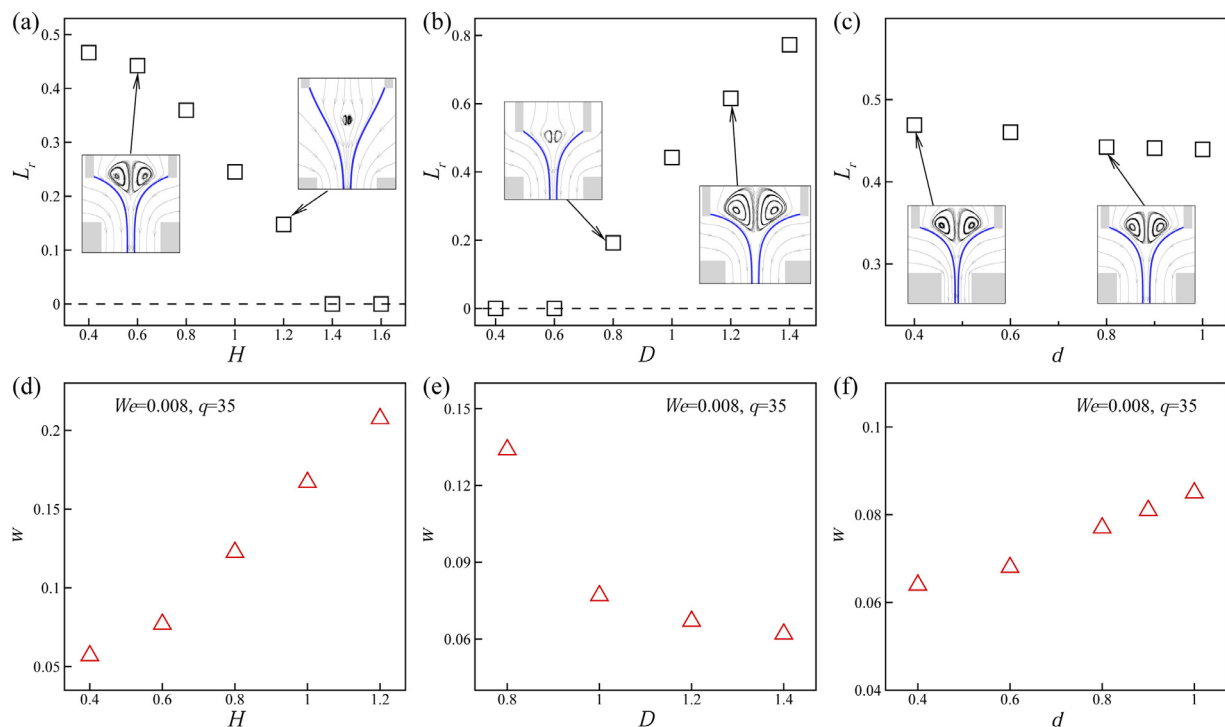


Fig. 10. Length of recirculation cell L_r and gaps between the recirculation cell and the interface w under $r_{\mu}=5$, $We=0.008$ and $q=35$, where (a) and (d) denotes the change of the distance H between the capillary tube and orifice, (b) and (e) denotes the change of the capillary tube diameter D , (c) and (f) denotes the change of the orifice diameter d , respectively.

focusing liquids simultaneously, thus it only affect the size of the RC and the gap slightly.

4. Conclusion

The effect of various control parameters on the liquid cone in a LL-FF process is studied in this work. Scaling analysis which considers the balance between the viscous shear stress and the interfacial tension at the cone shows that the instability of liquid cone is dominated by various parameters collectively. For example, an increase of the focused and focusing liquid flow rates and the liquid viscosity can promote a more stable cone, while the increase of interfacial tension and the orifice diameter and the distance between the capillary tube and the orifice plays the opposite effect. The experimental and numerical results validate the predictions of scaling law, and further study the effect of various parameters on the interface morphology and flow field of the cone. The numerical results show that the recirculation flow pattern may occur inside the cone at a relative high viscosity ratio between the focusing and focused liquid, and the size of the recirculation flow would increase with the viscosity ratio. Quantitative analysis on the flow fields show that the occurrence of recirculation flow is directly related to the balance of local shear stress on the cone interface. Under a high viscosity ratio, the size of recirculation flow can be further affected by the flow rates and geometry parameters as the local flow velocities are manipulated by these parameters. This work serves as a guideline to the optimization of control parameters in flow focusing, and contributes to the production of microdroplets based on a stable cone-jet geometry.

Declaration of Competing Interest

The authors declare that they have no known competing financial interests or personal relationships that could have appeared to influence the work reported in this paper.

CRediT authorship contribution statement

Kai Mu: Conceptualization, Methodology, Writing - original draft. **Ran Qiao:** Software, Validation. **Jianfeng Guo:** Data curation, Formal analysis. **Chaoyu Yang:** Investigation. **Yanfeng Wu:** Writing - review & editing, Project administration. **Ting Si:** Writing - review & editing, Funding acquisition.

Acknowledgments

This work is supported by the National Natural Science Foundation of China (Nos. 11722222, 11621202 and 11902318), the Strategic Priority Research Program of the Chinese Academy of Sciences (No. XDB22040403), the Youth Innovation Promotion Association CAS (No. 2018491) and the Fundamental Research Funds for the Central Universities. The authors would like to express their appreciation to Prof. Hang Ding for the support of computing resource and helpful discussions.

Supplementary material

See the supplementary material for more details on the dynamic characteristics of the RC. Video S1: numerical simulations for the movement of marked particles and the streamlines inside the cone. Video S2: experimental visualization of RC through adding hollow glass beads for the focused liquid.

Supplementary material associated with this article can be found, in the online version, at doi:[10.1016/j.ijmultiphaseflow.2020.103507](https://doi.org/10.1016/j.ijmultiphaseflow.2020.103507).

References

- Anna, S.L., 2016. Droplets and bubbles in microfluidic devices. *Annu. Rev. Fluid Mech.* 48, 285–309.
- Anna, S.L., Mayer, H.C., 2006. Microscale tip-streaming in a microfluidic flow focusing device. *Phys. Fluids* 18, 121512.

- Barrero, A., Loscertales, I.G., 2007. Micro- and nanoparticles via capillary flows. *Annu. Rev. Fluid Mech.* 39, 89–106.
- Blanco-Trejo, S., Herrada, M., Gañán-Calvo, A., Rubio, A., Cabezas, M., Montanero, J., 2020. Whipping in gaseous flow focusing. *Int. J. Multiphase Flow* 130, 103367.
- Castro-Hernandez, E., Gundabala, V., Fernandez-Nieves, A., Gordillo, J.M., 2009. Scaling the drop size in coflow experiments. *New J. Phys.* 11, 075021.
- Chattopadhyay, C., Gañán-Calvo, A.M., 2019. Spatio-temporal instability of two superposed fluids in a channel with boundary slip. *Int. J. Multiphase Flow* 113, 264–278.
- Christopher, G.F., Anna, S.L., 2007. Microfluidic methods for generating continuous droplet streams. *J. Phys. D: Appl. Phys.* 40, 319–336.
- Cruz-Mazo, F., Montanero, J.M., Gañán-Calvo, A.M., 2016. Monosized dripping mode of axisymmetric flow focusing. *Phys. Rev. E* 94, 053122.
- Ding, H., Spelt, P.D.M., 2007. Wetting condition in diffuse interface simulations of contact line motion. *Phys. Rev. E* 75, 46708.
- Ding, H., Spelt, P.D.M., Shu, C., 2007. Diffuse interface model for incompressible two-phase flows with large density ratios. *J. Comput. Phys.* 226, 2078–2095.
- Eggers, J., Villermaux, E., 2008. Physics of liquid jets. *Rep. Prog. Phys.* 71, 036601.
- Gañán-Calvo, A.M., 1998. Generation of steady liquid microthreads and micron-sized monodisperse sprays in gas streams. *Phys. Rev. Lett.* 80, 285–288.
- Gañán-Calvo, A.M., 2005. Enhanced liquid atomization: From flow-focusing to flow-blurring. *Appl. Phys. Lett.* 86, 214101.
- Gañán-Calvo, A.M., Ferrera, C., Torregrosa, M., Herrada, M.A., Marchand, M., 2011. Experimental and numerical study of the recirculation flow inside a liquid meniscus focused by air. *Microfluid. Nanofluid.* 11, 65–74.
- Gañán-Calvo, A.M., Gordillo, J.M., 2001. Perfectly monodisperse microbubbling by capillary flow focusing. *Phys. Rev. Lett.* 87, 274501.
- Gañán-Calvo, A.M., Montanero, J.M., Martín-Banderas, L., Flores-Mosquera, M., 2013. Building functional materials for health care and pharmacy from microfluidic principles and flow focusing. *Adv. Drug Deliv. Rev.* 65, 1447–1469.
- Gañán-Calvo, A.M., Riesco-Chueca, P., 2006. Jetting-dripping transition of a liquid jet in a lower viscosity co-flowing immiscible liquid: The minimum flow rate in flow focusing. *J. Fluid Mech.* 553, 75–84.
- Gordillo, J.M., Gañán-Calvo, A.M., Perez-Saborid, M., 2001. Monodisperse microbubbling: Absolute instabilities in coflowing gas-liquid jets. *Phys. Fluids* 13, 3839–3842.
- Herrada, M.A., Gañán-Calvo, A.M., Ojeda-Monge, A., 2008. Liquid flow focused by a gas: Jetting, dripping, and recirculation. *Phys. Rev. E* 78, 036323.
- Lee, W., Walker, M., Anna, S.L., 2009. Role of geometry and fluid properties in droplet and thread formation processes in planar flow focusing. *Phys. Fluids* 21, 032103.
- Liu, H.R., Mu, K., Ding, H., 2016. Simulation of incompressible multiphase flows with complex geometry using etching multiblock method. *Appl. Math. Mech.* 37, 1405–1418.
- Magaletti, F., Francesco, P., Chinappi, M., Marino, L., Casciola, C.M., 2013. The sharp-interface limit of the cahn-hilliard/navier-stokes model for binary fluids. *J. Fluid Mech.* 714, 95–126.
- Montanero, J.M., Rebollo-Munoz, N., Herrada, M.A., Gañán-Calvo, A.M., 2011. Global stability of the focusing effect of fluid jet flows. *Phys. Rev. E* 83, 036309.
- Mu, K., Ding, H., Si, T., 2018. Instability analysis of the cone-jet flow in liquid driven flow focusing. *Microfluid. Nanofluid.* 22, 138.
- Mu, K., Ding, H., Si, T., 2020. Experimental and numerical investigations on interface coupling of coaxial liquid jets in co-flow focusing. *Phys. Fluids* 32, 042103.
- Mu, K., Si, T., Ding, H., 2019. Nonlinear dynamics and manipulation of dripping in capillary flow focusing. *Sci. China Phys. Mech.* 62, 124713.
- Mu, K., Si, T., Li, E.Q., Xu, R.X., Ding, H., 2018. Numerical study on droplet generation in axisymmetric flow focusing upon actuation. *Phys. Fluids* 30, 012111.
- Nunes, J.K., Tsai, S.S.H., Wan, J., Stone, H.A., 2013. Dripping and jetting in microfluidic multiphase flows applied to particle and fibre synthesis. *J. Phys. D: Appl. Phys.* 46, 114002.
- Pang, Y., Du, Y., Wang, J., Liu, Z.M., 2019. Generation of single/double janus emulsion droplets in co-flowing microtube. *Int. J. Multiphase Flow* 113, 199–207.
- Si, T., Feng, H.X., Luo, X.S., Xu, R.X., 2015. Formation of steady compound cone-jet modes and multilayered droplets in a triaxial capillary flow focusing device. *Microfluid. Nanofluid.* 18, 967–977.
- Si, T., Li, F., Yin, X.Y., Yin, X.Z., 2009. Modes in flow focusing and instability of coaxial liquid jets. *J. Fluid Mech.* 629, 1–23.
- Si, T., Li, F., Yin, X.Y., Yin, X.Z., 2010. Spatial instability of co-flowing liquid-gas jets in capillary flow focusing. *Phys. Fluids* 22, 112105.
- Si, T., Li, G.B., Yin, X.Z., 2017. Coaxial jet and flow focusing. *Adv. Mech.* 47, 201701.
- Si, T., Yin, C.S., Gao, P., Li, G.B., Ding, H., He, X.M., Xie, B., Xu, R.X., 2016. Steady cone-jet mode in compound-fluidic electro-flow focusing for fabricating multi-compartment microcapsules. *Appl. Phys. Lett.* 108, 021601.
- Wang, Z.B., Zhai, T.Q., Liu, H.Y., Huang, Y.A., Deng, W.W., 2020. Two dimensional liquid flow focusing. *Phys. Fluids* 32, 042104.
- Wu, Q., Yang, C.Y., Yang, J.X., Huang, F.S., Liu, G.L., Zhu, Z.Q., Si, T., Xu, R.X., 2018. Photopolymerization of complex emulsions with irregular shapes fabricated by multiplex coaxial flow focusing. *Appl. Phys. Lett.* 112, 071601.
- Yang, C.Y., Qian, R., Mu, K., Zhu, Z.Q., Xu, R.X., Si, T., 2019. Manipulation of jet breakup length and droplet size in axisymmetric flow focusing upon actuation. *Phys. Fluids* 31, 019702.
- Zeguai, S., Chikh, S., Tadrist, L., 2020. Experimental study of air-water two-phase flow pattern evolution in a mini tube: Influence of tube orientation with respect to gravity. *Int. J. Multiphase Flow* 132, 103413.
- Zhang, C., Weldetsadik, N.T., Hayat, Z., Fu, T.T., Zhu, C.Y., Jiang, S.K., Ma, Y.G., 2019. The effect of liquid viscosity on bubble formation dynamics in a flow-focusing device. *Int. J. Multiphase Flow* 117, 206–211.
- Zhao, J., Ning, Z., Lv, M., Wang, G., 2019. Numerical simulation of flow focusing pattern and morphological changes in two-phase flow inside nozzle. *Chinese J. Chem. Eng.* 27, 63–71.
- Zhao, Y.P., 2012. Physical mechanics of surfaces and interfaces. Beijing: Science Press.
- Zhu, P.A., Wang, L.Q., 2017. Passive and active droplet generation with microfluidics: a review. *Lab Chip* 17, 34–75.